ACS APPLIED ELECTRONIC MATERIALS

pubs.acs.org/acsaelm Article

Magnetism and Magnetoelectricity of Textured Polycrystalline Bulk Cr_2O_3 Sintered in Conditions Far out of Equilibrium

Igor Veremchuk,* Pavlo Makushko, Natascha Hedrich, Yevhen Zabila, Tobias Kosub, Maciej Oskar Liedke, Maik Butterling, Ahmed G. Attallah, Andreas Wagner, Ulrich Burkhardt, Oleksandr V. Pylypovskyi, René Hübner, Juergen Fassbender, Patrick Maletinsky, and Denys Makarov*

Cite This: ACS Appl. Electron. Mater. 2022, 4, 2943−2952 Read Online

ACCESS | Metrics & More | Article Recommendations | Supporting Information

ABSTRACT: Magnetoelectric antiferromagnets like Cr_2O_3 are attractive for the realization of energy-efficient and high-speed spin−orbitronic-based memory devices. Here, we demonstrate that the fabrication of polycrystalline bulk Cr_2O_3 samples in conditions far out of equilibrium relying on spark plasma sintering allows high-quality material with a density close to that of a single crystal to be realized. The sintered sample possesses a preferential [0001] texture at the surface, which can be attributed to uniaxial strain applied to the sample during the sintering process. The antiferromagnetic state of the sample and linear magnetoelectric effect are accessed all-electrically relying on the spin Hall magnetoresistance effect in the Pt electrode interfaced with Cr_2O_3. In line with the integral magnetometry measurements, the magnetotransport characterization reveals that the sample possesses the magnetic phase transition temperature of about 308 K, which is the same as in a single crystal. The antiferromagnetic domain pattern consists of small domains with sizes in the range of only several micrometers, which is formed due to the granular structure of the sample. The possibility to access the magnetoelectric properties of the samples relying on magnetotransport measurements indicates the potential of the polycrystalline Cr_2O_3 samples for prospective research in antiferromagnetic spintronics.

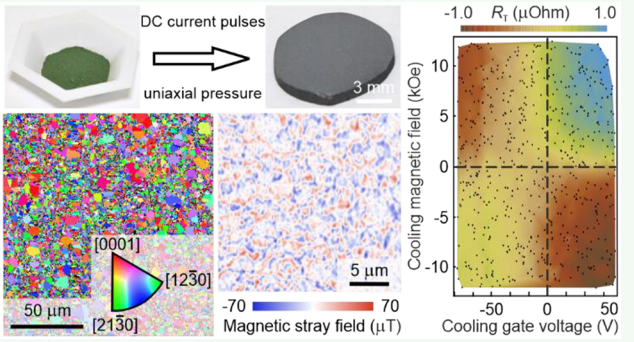

KEYWORDS: *magnetoelectric, antiferromagnet, Cr_2O_3, magnetotransport, spark plasma sintering*

INTRODUCTION

Magnetoelectric Cr_2O_3 is a collinear antiferromagnetic insulator below its Néel temperature of about 307 K.[1,2] It is also a room-temperature magnetoelectric material with uniaxial anisotropy, which makes it a candidate material for magnetoelectric random access memory (MERAM)[3] and purely antiferromagnetic MERAM (AF-MERAM)[4] as well as for data storage concepts relying on antiferromagnetic domain walls.[5] Recently, it was shown that B-doping of Cr_2O_3 thin films can control the nonvolatile rotation of the Néel vector up to 400 K by an electric field only due to the indirect coupling between electric polarization and antiferromagnetic order parameter.[6] With this work, one of the major issues of Cr_2O_3, namely, its comparatively low Néel temperature, is successfully addressed. We note that, due to the linear magnetoelectric effect, the magnetic order parameter in Cr_2O_3 can be switched by the electric field applied to the antiferromagnetic insulator. This paves the way toward energy efficient prospective memory devices based on antiferromagnets. In addition to magnetoelectric manipulation of the order parameter as in Cr_2O_3, there are alternative concepts exploring strain effects and spin(orbit)torques applied to metallic and insulating antiferromagnets.[7−9] For a review of different electric field controls, see ref 10.

In contrast to single crystals and textured thin films, there are no reports on the spintronic performance of devices based on cost-efficient polycrystalline bulk Cr_2O_3. To this end, it is known that a hot-pressed polycrystalline Cr_2O_3 material reveals a sizable magnetoelectric effect, which is only about 3 times smaller than the one of a single crystal.[11−13] We would like to note that the symmetry of the magnetoelectric (ME) effect does not allow the ME tensor average to be zero for powders independently of the presence or absence of the preferred texture. For example, for the random distribution of grains in the powder and parallel electric and magnetic fields, the ME effect in Cr_2O_3 is isotropic.[11] More recent theoretical

Received: March 28, 2022
Accepted: May 29, 2022
Published: June 13, 2022

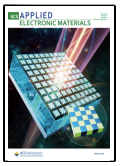

https://doi.org/10.1021/acsaelm.2c00398
ACS Appl. Electron. Mater. 2022, 4, 2943−2952

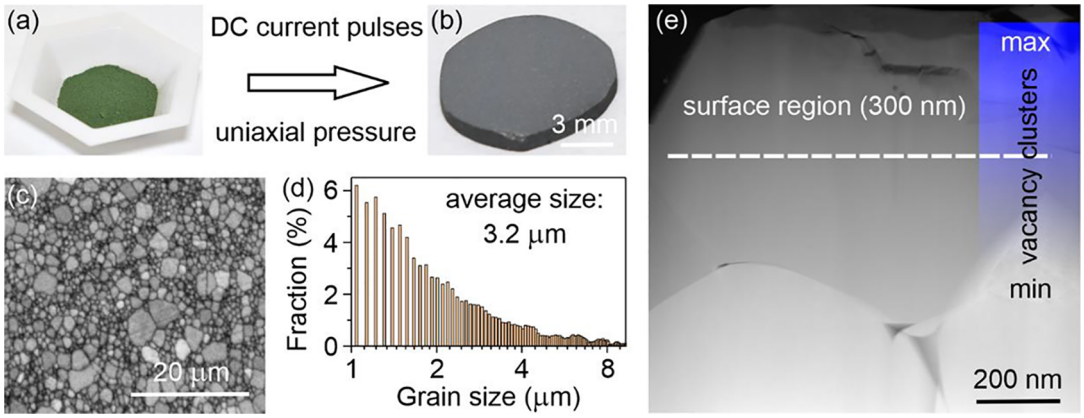

Figure 1. Fabrication and microstructure of SPS-sintered Cr_2O_3. (a) Cr_2O_3 powder is sintered by SPS using dc current pulses under uniaxial applied pressure to obtain (b) a dense Cr_2O_3 pellet with a diameter of 10 mm. (c) SEM image of the top surface of the SPS-sintered pellet. (d) Statistics on the grain sizes performed by the analysis of the data shown in panel (c). (e) High-angle annular dark-field scanning transition electron microscopy (HAADF-STEM) image of the cross-sectional lamella of the SPS-sintered Cr_2O_3 sample. (inset) The schematic represents the accumulation of small volume defects at the subsurface region of the sample. Deeper than 300 nm, individual grains behave as a single crystal in terms of small volume defects.

models, which take into account intergrain interaction and assume the Gaussian distribution of the orientation distribution function, allow one to obtain a good coincidence between analytics and experimental data. In particular, the longitudinal and transversal components of the ME tensor are reduced and enhanced, respectively.[12,13] Although a sizable ME coefficient is relevant for spintronic devices, by now, polycrystalline bulk materials are not implemented in spintronics research. For instance, it is not demonstrated yet that polycrystalline bulk Cr_2O_3 can be fabricated in a quality that is sufficient for all-electrical readout of the antiferromagnetic order parameter as would be needed for practical applications in spintronics. Furthermore, it is not known if all-electrically it could be possible to manipulate the order parameter using electric fields as would be needed for energy efficient magnetic memory applications. Another important aspect is the random orientation of crystallites that limits the attractiveness of polycrystalline antiferromagnets for research on antiferromagnetic spintronics.[14,15] The randomness of grain orientations is a direct consequence of the fabrication methods relying on the sample preparation at conditions close to thermodynamic equilibrium.[16,17]

Here, we fabricate dense polycrystalline Cr_2O_3 samples at conditions far out of equilibrium relying on the spark plasma sintering (SPS) technique.[18,19] The SPS is based on direct-current (dc) pulses and uniaxial pressure applied to a powder material, thus imposing an axial strain to the sintered material. The analysis of the temperature dependent magnetic susceptibility and grain orientations at the surface of the sintered samples indicates a preferential [0001] texture. We study integral magnetic properties of the samples using superconductive quantum interference device vibrating sample magnetometry (SQUID-VSM) and locally measure the temperature evolution of the antiferromagnetic domain patterns using scanning nitrogen vacancy (NV) center magnetometry. Furthermore, we address the magnetoelectric switching performance relying on magnetotransport measurements. Sintered Cr_2O_3 pellets exhibit the Néel temperature of about 308 K and possess micrometer-size antiferromagnetic domains. Magnetotransport measurements relying on the spin Hall effect in a Pt electrode in proximity to the polycrystalline Cr_2O_3 confirm the linear magnetoelectric effect in the material. The all-electrical access of the magnetoelectric responses of polycrystalline Cr_2O_3 paves the way toward spintronic and spin−orbitronic devices based on this inexpensive material prepared by industry-scale methods.

RESULTS AND DISCUSSION

For sample preparation, we used a commercially available Cr_2O_3 powder (Figures 1a and S1), which was sintered by SPS at 1573 K under uniaxial pressure of 30 MPa in an Ar atmosphere. We prepared Cr_2O_3 pellets with a thickness of 0.5 mm and a diameter of 10 mm (Figure 1b). After synthesis, the top surface of the sample was mechanically polished (surface roughness of about 10 nm). In contrast to established fabrication methods,[11] the SPS technique allowed us to obtain Cr_2O_3 pellets with a mass density of 99.5% of the theoretical density, which renders the physical properties of the samples close to those of single crystals. X-ray diffraction studies confirm that SPS-processed samples are single phase with the corundum-type crystal structure (space group $R\bar{3}c$, a = 4.9585(1) Å, c = 13.5934(3) Å at 293 K; see Figure S2). Microstructural investigations were done using scanning electron microscopy (SEM) for the top surface characterization (Figures 1c,d and S3) and transmission electron microscopy (TEM) for cross-sectional studies (Figures 1e, S4, and S5). The sintered sample consists of grains with a typical size of 1 to 5 μm (Figure 1c−e), each possessing the corundum-type structure of Cr_2O_3 as confirmed via electron diffraction analysis (Figure S4). Depth profiling of small volume defects of the polished Cr_2O_3 pellet was carried out using positron annihilation spectroscopy (PAS). From Doppler broadening PAS (Figure S6a), an effective positron diffusion length (L_+) of 99.1 ± 0.6 nm was estimated, allowing for calculation of the overall defect concentration of $c_V \approx 0.66$ ppm. The positron annihilation lifetime spectroscopy (PALS) analysis, on the other hand, revealed that, in the subsurface region of the sample within the topmost ∼300 nm, there are defect clusters of about 7 vacancies in individual Cr_2O_3 grains (inset in Figure 1e; see also Figure S6b,c). The cluster size was defined from the comparison of the experimental PALS data with the density functional theory (DFT) calculations carried

https://doi.org/10.1021/acsaelm.2c00398
ACS Appl. Electron. Mater. 2022, 4, 2943−2952

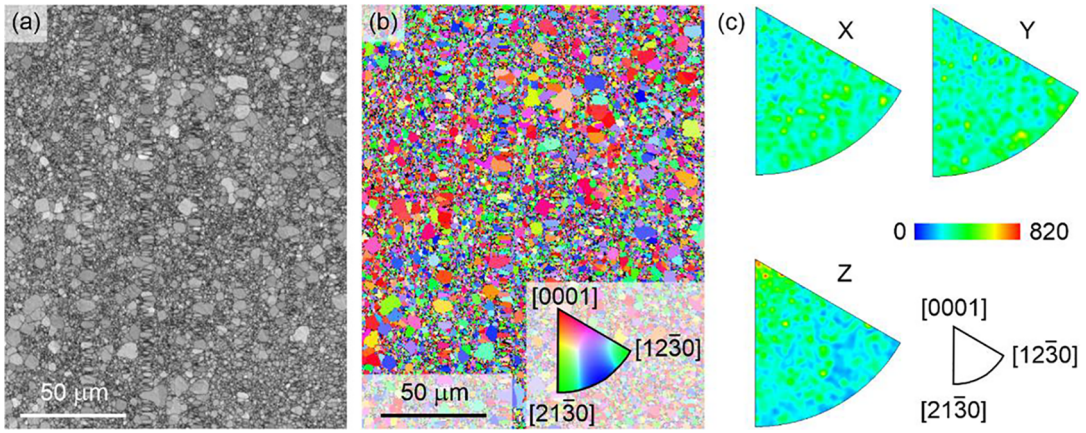

Figure 2. Characterization of the orientation of grains at the surface. (a) EBSD quality map. (b) Grain orientation map (inverse pole figure Z) showing the color coded crystallographic direction $\{uv(\overline{u+v})w\}$, which is parallel to the sample surface normal. The color code is given in the inset. (c) Frequency distribution of the crystallographic direction $\{uv(\overline{u+v})w\}$ along *X*, *Y*, and *Z*. Scaling is according to the color bar.

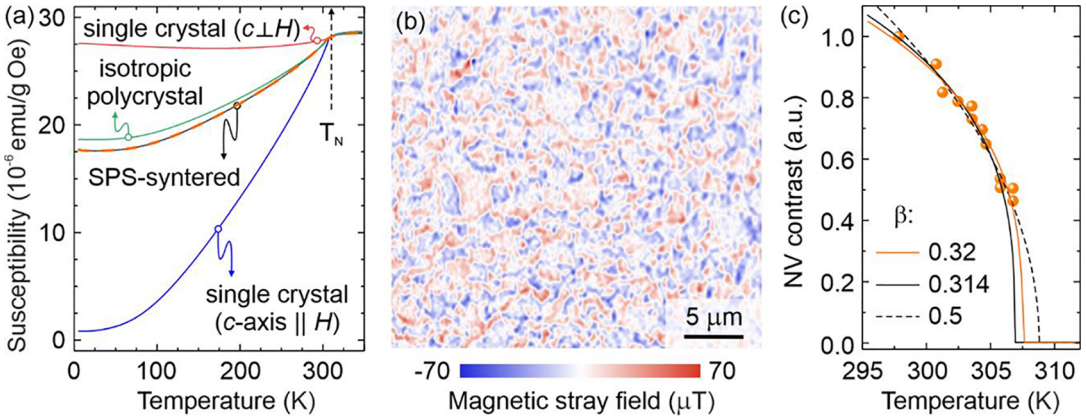

Figure 3. Magnetic characterization. (a) The magnetic susceptibility of the SPS-sintered sample (black curve) and of a single crystalline Cr_2O_3 sample measured with the magnetic field of 100 Oe applied along (blue curve) and perpendicular (red curve) to the *c*-axis of the sample. The SPS-processed samples is measured in the geometry when the magnetic field is applied perpendicular to the surface of the pellet. (b) Scanning NV magnetometry investigation of the antiferromagnetic domain pattern in the SPS-sintered Cr_2O_3 sample. The measurement is carried out at 295 K. (c) Estimation of the magnetic phase transition temperature from the temperature dependent evolution of the magnetic stray fields measured using NV magnetometry. Symbols correspond to the NV data (Figure S8). Solid orange curve is a fit to the NV data using the power law $[1-(T/T_N)^3]^\beta$ calculated for the fixed T_N = 307.5 K (estimated from the SQUID-VSM data, panel (a)) taking β as a free parameter. The best fit gives β = 0.32. For comparison, we also show fits to the same equation with the fixed critical exponents [β = 0.314 (3D Ising universality class; solid black curve) and β = 0.5 (mean field approximation; dashed black curve)] with T_N taken as a fitting parameter.

out for Cr_2O_3 (Figure S6d). It should be noted that the vacancy clusters could be located at grain boundaries as well. Deeper than 300 nm, the concentration of small volume defects is likely even smaller when the unsaturated behavior of the positron lifetimes is considered. This finding indicates a high quality of individual Cr_2O_3 grains in the interior of the sample.

To access the texture of the samples, we performed electron backscatter diffraction (EBSD) investigations of the SPS-sintered polycrystalline Cr_2O_3 (Figure 2). All crystallites show different crystallographic orientations (Figure 2b), and the standard EBSD analysis revealed no further orientation variation within each crystal (Figure 2b,c). The texture analysis demonstrates a preferred orientation of the [0001] direction of the Cr_2O_3 unit cell parallel to the sample surface normal (Figure 2c). The formation of preferentially [0001]-oriented grains in polycrystalline Cr_2O_3 samples was not reported before. We consider that the axial strain applied to the sample during the SPS process can act as a driving force for the formation of the preferential [0001] texture. In analogy with Al_2O_3, the uniaxial pressure used during the SPS process results in a deformation at high temperatures, leading to the crystallographic slip of individual grains.[20]

There are independent slip planes in corundum structure at high temperatures, namely, (0001) $\langle 11\bar{2}0\rangle$, $(1\bar{2}10)$ $\langle 10\bar{1}0\rangle$, $(1\bar{2}10)$ $\langle 10\bar{1}1\rangle$, $(1\bar{1}02)$ $\langle 01\bar{1}1\rangle$, and $(10\bar{1}1)$ $\langle 01\bar{1}1\rangle$.[21] Consequently, to accommodate a significant axial strain under SPS conditions, a possible rotation of the grains having the (0001) plane oriented perpendicular to the uniaxial pressure may occur.[20] We anticipate that this mechanism could be responsible for the development of the [0001] texture in our Cr_2O_3 samples. Furthermore, theoretical calculations have shown that thermodynamically favored orientation slides (0001) withstand uniaxial pressure during the SPS process.[22−24] Therefore, complementary effects including recrystallization, dislocation slip, grain boundary sliding, and anisotropic grain growth could contribute to the texture formation in Cr_2O_3 similar to the case of SPS-processed polycrystalline

https://doi.org/10.1021/acsaelm.2c00398
ACS Appl. Electron. Mater. 2022, 4, 2943−2952

Al_2O_3.[25] Further in depth theoretical and experimental studies are needed to understand the texture formation in SPS-processed Cr_2O_3 powder.

Integral magnetic properties of the samples were studied using SQUID-VSM. The magnetic susceptibility, χ, measurements revealed the antiferromagnet−paramagnet transition temperature (Néel temperature, T_N) of 307.5 ± 2 K, which corresponds to the T_N of a single crystal[26] (Figure 3a). The temperature dependence of the magnetic susceptibility of the *isotropic* polycrystalline sample (green curve, which is calculated as $(2/3\chi_{perp} + 1/3\chi_{para})$) can be represented as a combination of magnetic susceptibilities of a single crystal measured with a magnetic field applied in the direction parallel (blue curve, χ_{para}) and perpendicular (red curve, χ_{perp}) to the [0001] direction.[26] The magnetic susceptibility of the SPS-sintered Cr_2O_3 sample (black curve) does not coincide with the one for the isotropic polycrystal and is closer to the curve corresponding to the single crystal measured with the magnetic field applied along the [0001] orientation. Since the magnetic susceptibility is the bulk quantity, it is reasonable to assume that the degree of [0001] texture should be related to the deviation of the susceptibility from the isotropic case (black curve in Figure 3a moves closer to the blue curve). From the EBSD data (Figure 2), we know that the sample reveals about 10% of [0001] texture. We assume that it is possible to introduce a correction to the equation of the isotropic case (green curve in Figure 3a) to assess if the degree of the [0001] texture corresponds to the shift of the measured curve for the SPS-processed sample (black curve in Figure 3a) toward the single crystal characterized in an external magnetic field applied parallel to the *c*-axis (blue curve in Figure 3a). As one possible way to introduce such a correction, we rewrite the susceptibility for the isotropic sample as $[(2/3 - \zeta)\chi_{perp} + (1/3 + \zeta)\chi_{para}]$ with an adjustment parameter ζ. By fitting the latter equation to the experimental data (black curve in Figure 3a), we derive that the adjustment parameter ζ is equal to about 0.032 (dashed orange curve in Figure 3a), which is about 10% of the contribution of the [0001] texture for the case of the ideal isotropic sample (1/3).

We analyzed the magnetic domain pattern of the SPS-processed sample using scanning NV magnetometry, which allows one to measure the spatial map of magnetic stray fields at the nanoscale.[27,28] This is the very first imaging of the antiferromagnetic domain pattern of a polycrystalline bulk Cr_2O_3 sample. The scanning NV magnetometry studies performed at 295 K after zero field cooling reveal a complex multidomain state with characteristic magnetic domain sizes in the range of 1−5 μm (Figure 3b). The domain pattern differs substantially from the one taken for a single-crystalline sample[5,29] with large mm-sized domains. In the case of the SPS-processed sample, antiferromagnetic domain walls are pinned at defects like grain boundaries resulting in a pattern, which is similar to those observed in textured Cr_2O_3 thin films.[30] We note that the resolution of the scanning NV magnetometry was not sufficient to unambiguously claim that domain walls are exclusively pinned at grain boundaries. Still, we do see correlation between the domain size and the grain size, which allows us to expect that antiferromagnetic domain walls in Cr_2O_3 "feel" grain boundaries. Indeed, NV data allows us to estimate a characteristic magnetic domain size on the order of several micrometers (Figure 3b), which is similar to the typical grain size of the sintered sample (Figure 1c−e). To assess the pinning of domain walls on defects, we performed several temperature cycles (heating the sample to above the Néel temperature and cooling to the antiferromagnetically ordered state). This study allows us to check if the domain pattern reappears at the same location. The results are shown in Figure S7 (see also related Figures S8−S11). The data show that the domain pattern reappears yet is not exactly the same. The difference is seen via the reversal of the contrast at the location of certain domain walls (indicated regions in Figure S7). Still, the location of some domain walls remain the same (only contrast is reversed), indicating that the morphology of the domain pattern is dominated by the pinning of the antiferromagnetic domain walls at the structural defects. Considering that we do not have a correlation image where topography of the sample is superimposed with the antiferromagnetic domain pattern, we cannot exclude that domains are spread over several grains and are not confined to individual grains. This scenario could require at least a partial exchange coupling between Cr_2O_3 grains, which was already reported for the case of granular thin films of Cr_2O_3.[30]

To access the local antiferromagnet−paramagnet transition temperature, we follow the change of the contrast from the antiferromagnetic domain pattern by performing NV imaging of the sample at different temperatures (Figure S8). By fitting the temperature dependence of the NV contrast to the power law $[1 - (T/T_N)^3]^\beta$ (Figure 3c),[31] we determine the critical exponent β = 0.32 ± 0.05 for the fixed T_N = 307.5 K taken from the SQUID-VSM study (Figure 3a). The value for the critical exponent corresponds to the 3D Ising universality class as established for high quality Cr_2O_3 single crystals.[31] For completeness, in Figure 3c, we show two fit curves calculated for fixed critical exponents of β = 0.314 (3D Ising universality class) and β = 0.5 (mean field approximation) with T_N taken as a free fitting parameter. The best fit provides estimates for the Néel temperature of 307 K (for β = 0.314; solid black curve in Figure 3c) and 309 K (β = 0.5; dashed black curve in Figure 3c). Although both fit curves describe the experimental data well, the mean field model with β = 0.5 overestimates the Néel temperature compared to the SQUID-VSM data (Figure 3a). We further performed SQUID-VSM measurements of the uncompensated magnetic moment as a function of temperature for the SPS-processed sample (Figure S12). The fit of the experimental data to the power law indicated above carried out for the case of fixed critical exponents of β = 0.314 and 0.5 allows us to estimate the Néel temperature taken as a fitting parameter. The best fit to the SQUID-VSM data (Figure S12) gives a T_N of 306.6 K (for β = 0.314) and 307.5 K (for β = 0.5), which agree well with the susceptibility study (Figure 3a). Although the NV magnetometry measurements suggest that the 3D Ising universality class could give a better fit to the experimental data, the overall accuracy of the combined SQUID-VSM data (Figures 3a and S12) and NV data (Figures 3c and S7−S11) does not allow us to unambiguously determine the critical exponent for the SPS-processed sample.

Magnetotransport studies provide access to the magnetic phase transition temperature at the sample surface for different antiferromagnetic materials[32−36] and to the magnetoelectric effect in Cr_2O_3.[4,6,37] For these studies, the SPS-processed Cr_2O_3 pellet was capped with a 5 nm-thick Pt film, which was then contacted at four points for transverse resistance measurements carried out by exposing the sample to the out-of-plane magnetic field (Figure 4a). There are several mechanisms that can lead to the change of the transverse resistance of the Pt film, R_T, interfaced with Cr_2O_3 including

https://doi.org/10.1021/acsaelm.2c00398
ACS Appl. Electron. Mater. 2022, 4, 2943−2952

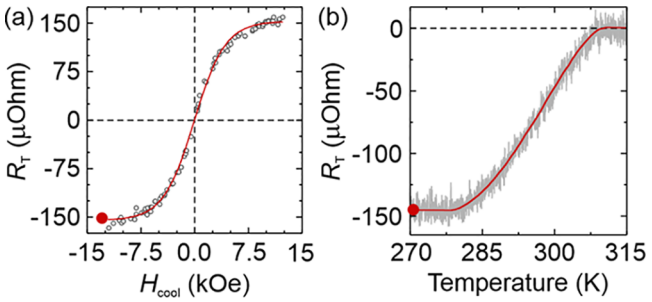

Figure 4. Magnetotransport characterization of the SPS-sintered Cr_2O_3. (a) Measurement of the transverse resistance change, R_T, of a Pt capping layer as a function of the cooling magnetic field applied perpendicular to the sample plane. The measurement is carried out at remanence at 270 K after the sample was cooled from 320 K in an applied magnetic field H_{cool}. (b) Zero-field-warming experiment where R_T is measured upon warming the sample from 270 K after it was cooled in the cooling field of −15 kOe. At the transition temperature of about 308 K, the measured signal vanishes. In both panels, red solid curves are guides to the eye. The red circle in both panels indicates that the initial condition for the zero-field-warming experiment (panel (b)) is prepared in the field cooling experiment shown in panel (a).

the spin Hall magnetoresistance effect[36] and magnetic moment at the Pt/Cr_2O_3 interface.[38] When cooling the sample to the temperature of choice in an external magnetic field of certain strength (named here as the cooling magnetic field, H_{cool}), the magnetic state of Cr_2O_3 adapts, leading to a predominant stabilization of the antiferromagnetic state along the cooling field direction. This dominance of one antiferromagnetic domain leads to a spontaneous transverse resistance in the Pt layer, even in a zero magnetic field (Figure 4a). We access the transition temperature in the transport measurement by performing the zero-field-warming experiment where the transverse resistance is measured upon warming the sample up from 270 to 320 K after it was cooled in the cooling field of −15 kOe. At the temperature of about 308 ± 2 K, the signal vanishes (Figure 4b). This temperature corresponds to the Néel temperature measured using SQUID-VSM. Therefore, we confirm that, also for the SPS-sintered Cr_2O_3 sample, the magnetotransport characterization provides access to the antiferromagnetic order parameter. We note that the criticality behavior measured using magnetotransport (Figure 4b) and NV magnetometry (Figure 3c) are different. This can be caused by the different defect nanostructures of the top surface region of the sample compared to the interior of the sample. Indeed, magnetotransport is a surface sensitive method, which does not allow us to probe bulk properties directly (unlike NV as well as SQUID-VSM magnetometry). For our SPS-processed sample, we know from the PAS analysis (see discussion related to Figures 1e and S6) that the top 65 nm of the sample contains various defects. As it was shown for the case of Cr_2O_3 thin films,[39] different type of defects located on the interface between Cr_2O_3 and Pt, as well as their concentration, have a significant influence on the behavior of the transversal resistance and its response to the external magnetic field.

One of the technologically relevant properties of Cr_2O_3 is its linear magnetoelectric effect, which allows for the electric field control of the antiferromagnetic order parameter. The magnetoelectric performance of the sample is presented as the dependence of the transverse resistance measured after the magnetoelectric field cooling. In this study, the sample is cooled through the Néel temperature from 320 down to 270 K in the presence of the collinear electric (E, realized by the applied cooling gate voltage, V_{cool}) and magnetic (H_{cool}) fields oriented perpendicular to the sample surface (Figure 5a). The

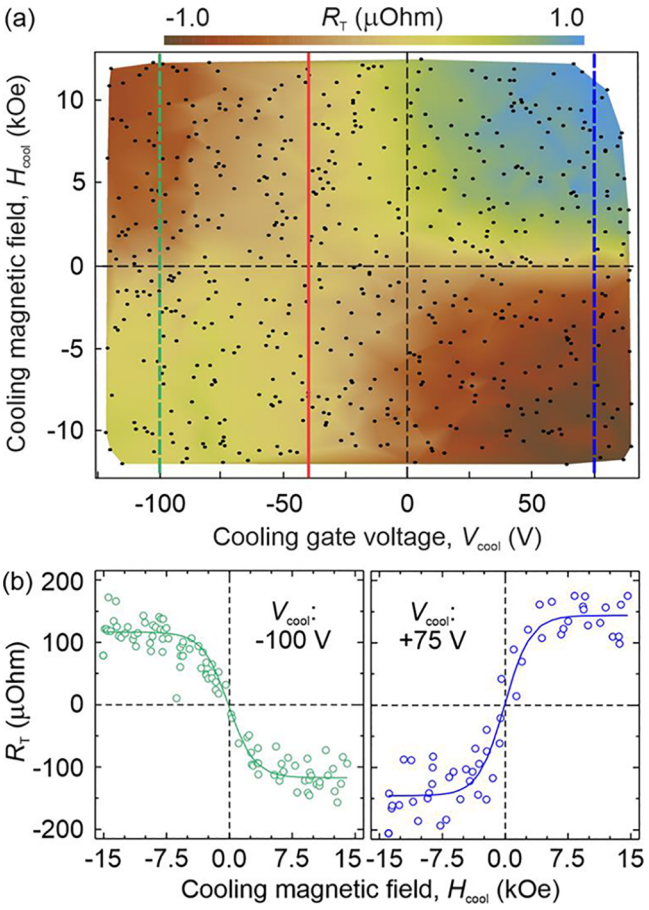

Figure 5. Magnetoeletric characterization of the SPS-sintered Cr_2O_3 sample. (a) Magnetoelectric map revealing the dependence of the transverse resistance, R_T, on the magnetoelectric field cooling (applied electric and magnetic fields). The electric field is controlled by applying cooling gate voltages, V_{cool}. Red solid line in panel (a) indicates the shift of the magnetoelectric map due to the gate bias voltage. (b) Line cuts through the magnetoelectric map shown in panel (a) at a selected V_{cool} of −100 V (indicated with a green dashed line in panel (a)) and +75 V (indicated with a blue dashed line in panel (a)). Solid curves in panel (b) are guides to the eye. All measurements were collected after the sample was cooled from 320 K through the antiferromagnetic ordering temperature to the measurement temperature of 270 K.

main trend of the magnetoelectric map is that, for the constant electric field, the transverse resistance increases and begins to saturate for strong cooling magnetic fields (Figure 5b). Furthermore, the change of the sign of the product of the EH fields leads to the sign reversal of the measured signal, which indicates the reversal of the antiferromagnetic order parameter.[4] The switching of the antiferromagnetic order parameters is consistent with that expected in Cr_2O_3 due to the linear magnetoelectric effect.[1−4,40,41] We note that, to the best of our knowledge, this is the first time the linear magnetoelectric effect of a polycrystalline Cr_2O_3 is measured using magnetotransport techniques. The EH-field symmetry of the

https://doi.org/10.1021/acsaelm.2c00398
ACS Appl. Electron. Mater. 2022, 4, 2943−2952

linear magnetoelectric effect is restored when accounting for a gate bias voltage,[4] which is about −45 V for this sample (indicated with the red line in Figure 5a). The gate bias voltage could be induced by defects in our polycrystalline SPS-fabricated Cr_2O_3 samples.[4,42−45] The magnetoelectric effect is also confirmed via the measurement of the exchange bias in the stack where the SPS-processed Cr_2O_3 sample is deposited with $[Co(0.4\ nm)/Pt(0.7\ nm)]_5$ multilayers (Figure S13). The possibility to affect the exchange bias using the magnetoelectric effect in Cr_2O_3 is in line with previous reports; see for instance refs 3 and 46.

CONCLUSION

We identify spark plasma sintering as a fabrication method to obtain fully dense polycrystalline Cr_2O_3. The SPS-sintered Cr_2O_3 samples reveal the same magnetic phase transition temperature of about 308 K as the corresponding single-crystalline material. In contrast to single crystals,[5] SPS-sintered samples possess an irregular antiferromagnetic domain pattern with a characteristic domain size of several micrometers. As the domain size is similar to the average grain size of Cr_2O_3 crystallites, we anticipate that grain boundaries can act as pinning sites for antiferromagnetic domain walls. The fundamental understanding of the mechanism of the domain wall pinning on structural defects in antiferromagnets represents an interesting prospective research direction. Furthermore, it is insightful to study the change of the antiferromagnetic domain pattern upon magnetoelectric manipulation.

The temperature dependence of the magnetic susceptibility as well as the EBSD analysis indicated a preferred orientation of the [0001] direction of the Cr_2O_3 unit cell parallel to the sample surface normal. We outlined several mechanisms, which can be responsible for the texture formation in SPS-processed Cr_2O_3 samples. In analogy to the isostructural Al_2O_3 compound, the uniaxial pressure applied to the Cr_2O_3 powder upon SPS processing might lead to the crystallographic slip of individual Cr_2O_3 grains resulting in a preferential [0001] texture. Our results are expected to stimulate further theoretical and experimental studies, which are needed to understand the mechanism of the texture formation in SPS-sintered Cr_2O_3 samples. This research could enable the realization of well textured Cr_2O_3 samples relying on the industry-scale cost- and time-efficient SPS fabrication method.

We perform magnetotransport measurements to access the surface Néel temperature (found to be the same as in the interior of the sample) as well as the linear magnetoelectric effect. For the latter, the simultaneous application of magnetic and electric fields while cooling the sample through the Néel temperature allows the antiferromagnetic order parameter to be switched, which is probed by measuring the spin Hall magnetoresistance effect in a Pt layer in proximity to Cr_2O_3. Our study enables the use of SPS-sintered bulk Cr_2O_3 samples for prospective spintronic and spin−orbitronic devices. Follow up research should include the validation of the possibility of *isothermal* switching of the antiferromagnetic order parameter and realization of AF-MERAM memory cells on this material. Furthermore, it is insightful to study the impact of the intergrain interaction on the magnetoelectricity.

METHODS

Spark Plasma Sintering (SPS). The SPS procedure was carried out in a protective argon atmosphere at a pressure of 1 atm (SPS: 515 S, Syntex-Fuji, Japan). Cr_2O_3 powder (Alfa Aesar) was placed into graphite dies with a diameter of 10 mm. The powder contains Cr_2O_3 particles with a broad size distribution (the maximum size of the particles is 22 μm determined by the used mesh). Graphite foil was used as a protective layer to avoid direct contact between the die and powder. A uniaxial pressure of 30 MPa and high electrical current pulses of 700 A (dc) were simultaneously applied to the graphite die filled with Cr_2O_3 powder. As Cr_2O_3 is an insulator, the electrical current in the form of dc pulses flows mainly through the graphite die, leading to the increase of its temperature (1573 K in this study) by the Joule heating effect. A major advantage of the SPS technique is a high heating rate of 100 K/min (in this study), leading to Cr_2O_3 grain growth and allowing for rapid compaction of the powder to highly dense pellets.

Powder X-ray Diffraction (PXRD). Phase identification was performed on the basis of the X-ray Guinier diffraction technique (Huber G670 camera, Cu Kα1 radiation, λ = 1.54056 Å, $\Delta 2\theta$ = 0.005°, 2θ range of 3.0° to 100°, exposure time of 6 × 15 min). The reflection positions obtained by profile deconvolution were corrected using the internal LaB_6 standard. Lattice and structure parameter refinements were performed with the program package WinCSD.[47] An attempt to use powder XRD for the characterization of the sample texture was not successful. The XRD pattern of the sample is shown in Figure S2. We analyzed the sample after SPS sintering, which is reprocessed in a powder form. We confirmed that the sample is single phase with the corundum-type crystal structure. The texture analysis includes a comparison of the intensity of relevant diffraction peaks. For instance, to determine the [0001] texture, we need to compare the intensity of all diffraction peaks with respect to the case of an ideally isotropic sample (without texture). This comparison is simulated in Figure S14a for the case of an isotropic sample (black pattern) and the same structural model but with 10% texture (as estimated from our EBSD study) along the [0001] direction (red pattern). The difference between the two patterns is shown in Figure S14b. The difference is very small, less than 3% of the maximum relative intensity. Now, we can compare the experimental XRD pattern taken of the powder sample (blue pattern), where we assume a random orientation of the particles with the isotropic model (black pattern; the same as in Figure S14a); please see Figure S14c. We note that the experimental XRD pattern was refined to have the smallest reliability factors (R_I for intensity and R_P for profile) with respect to the isotropic model (details on the refinement procedure are given ref 47). The difference between these best matched patterns is shown in Figure S14d. Next, we can compare the experimental XRD pattern taken of the powder sample (blue pattern; the same as in Figure S14c), where we assume a random orientation of the particles with the model pattern for the sample with 10% [0001] texture (red pattern; the same as in Figure S14a); please see Figure S14e. We note that the experimental XRD pattern was refined to have the smallest reliability factors (R_I for intensity and R_P for profile) with respect to the model with the 10% [0001] texture. The reliability factors remain low, which indicates that the quality of the structure refinement is good. The difference between these best matched patterns is shown in Figure S14f. The main issue is that the difference between the two models (Figure S14b) is 2−3 times smaller than the difference between experimental data and any of the assumed models (Figure S14d,f). Hence, no statement on the texture can be done on the basis of the results obtained using powder XRD. For this reason, for the texture analysis, we applied EBSD, which is established as an accurate and representative method for estimating the degree of predominant grain orientation. The results of the EBSD study are shown in Figure 2 of the main text.

Transmission Electron Microscopy (TEM). TEM analysis was conducted on thin cross sections of specimens after SPS processing. The cross sections were prepared by in situ lift-out using a Helios 5 CX focused ion beam (FIB) device (Thermo Fisher). To protect the sample surface, a carbon cap layer was deposited beginning with electron-beam-assisted and subsequently followed by Ga-FIB-assisted precursor decomposition. Afterward, the TEM lamella was prepared using a 30 keV Ga FIB with adapted currents. Its transfer to a 3-post

https://doi.org/10.1021/acsaelm.2c00398
ACS Appl. Electron. Mater. 2022, 4, 2943−2952

copper lift-out grid (Omniprobe) was done with an EasyLift EX nanomanipulator (Thermo Fisher). To minimize sidewall damage, Ga ions with only 5 keV energy were used for final thinning of the TEM lamella to electron transparency. Cross-sectional bright-field TEM imaging and selected-area electron diffraction were performed using an image-C_s-corrected Titan 80−300 microscope (FEI) operated at an accelerating voltage of 300 kV. High-angle annular dark-field scanning transmission electron microscopy (HAADF-STEM) imaging and spectrum imaging analysis based on energy-dispersive X-ray spectroscopy (EDXS) were performed with a Talos F200X microscope (FEI) operated at 200 kV. Prior to (S)TEM analysis, the specimen mounted on a high-visibility low-background holder was treated for 8 s with a Model 1020 Plasma Cleaner (Fischione) to remove possible contaminations.

Microstructural Analysis. For EBSD measurements, the sample was embedded in a conductive phenolic resin and metallographically prepared with the usual multistep grinding and polishing process. The measurements were performed in a scanning electron microscope (Jeol JSM 7800F) with an attached EBSD detector (Bruker CrystAlign System 400) at the acceleration voltage of 15 kV and excitation current of about 3 nA.

Integral Magnetic Characterization. These measurements were carried out on a single phase SPS-sintered sample as well as for a single-crystalline sample. In particular, a 1 mm-thick Cr_2O_3 single crystal (MaTecK) with [0001] surface orientation was used as a reference sample. Magnetic susceptibility was measured using SQUID-VSM in the temperature range from 4 to 400 K in the magnetic field of 100 Oe. For the measurement, the SPS-processed pellet was mounted with its normal along the field direction. To access the temperature dependence of the uncompensated moment in the SQUID-VSM (Figure S12), the following measurement protocol was applied: (i) the sample was heated to 400 K. Then, a magnetic field of +30 kOe was applied upon cooling the sample to the lowest measurement temperature. At this temperature, ac demagnetization of the solenoid magnet of the SQUID-VSM was carried out. After this, we measured the temperature dependence of the magnetic moment upon warming up the sample. (ii) The same process was repeated as described above, but the cooling field was set to −30 kOe. (iii) The uncompensated magnetic moment was calculated as a difference between the two measured magnetic moments.

Magnetotransport Measurements. We measured the transverse resistance, R_T, of the Pt thin film using a Tensormeter measurement device (HZDR Innovation GmbH). The transverse resistance is modified in a distinct way, allowing for the determination of the antiferromagnet−paramagnet phase transition temperature. After cooling the sample from 320 to 270 K in a magnetic field H_{cool}, we predominantly select one of two possible antiferromagnetic domains in the Cr_2O_3 sample. This dominance of one domain leads to the emergence of a spontaneous transverse resistance, even at a zero magnetic field. When heating the sample, this antiferromagnetic domain state decays and vanishes at the Néel temperature, as shown in Figure 4b. Ta foil (25 μm-thick) was used as a back-gate electrode. A source meter was used to apply a dc voltage in the range from −100 to +100 V between the Pt top electrode and the back-gate electrode.

Exchange Bias Study. We prepared an exchange biased stack by magnetron sputtering of substrate//Pt(0.5 nm)/[Co(0.4 nm)/Pt(0.7 nm)]$_5$/Pt(2 nm) on the SPS-sintered Cr_2O_3 sample. The thin film deposition was carried out at room temperature (base pressure: 5×10^{-8} mbar; Ar sputter pressure: 8×10^{-4} mbar; deposition rate: 0.1 nm/s). Before the thin film deposition, the Cr_2O_3 sample was annealed at 700 °C for 10 min in the vacuum chamber (Ar background pressure: 5×10^{-3} mbar). Exchange bias was measured using a zero offset Hall preset of a Tensormeter device (HZDR Innovation GmbH). For the measurement, the sample was supplied with a current of 5 mA. To access the exchange bias, the change of the transversal resistance was measured in the magnetic field applied in the out-of-plane direction at different temperatures from 288 to 320 K. Prior to the measurement of each hysteresis loop, the sample was heated to 335 K for 1 min and then cooled to the measurement temperature under applied external magnetic and electric fields. An electric field was applied between the Co/Pt stack (top metal layer) and the Cu back gate. The thickness of the Cr_2O_3 sample was 0.5 mm. The exchange bias performance is shown in Figure S13a−c for the sample annealed at a zero electric field and cooling magnetic field of +15 kOe. A clear shift of the magnetic hysteresis loop is observed (Figure S13a). The coercive field of the sample is about 140 Oe (Figure S13b). The exchange bias field at 288 K is about 20 Oe (Figure S13c). The magnetoelectric cooling of the sample was realized by applying a voltage of ±100 V in the magnetic field of +15 kOe (Figure S13d) and −15 kOe (Figure S1e). The sign of the magnetoelectric cooling field (positive for parallel and negative for antiparallel orientation of magnetic and electric fields) determines the sign of the exchange bias field; i.e., a positive (negative) shift of the hysteresis loop is observed for a positive (negative) magnetoelectric cooling field.

Positron Annihilation Spectroscopy (PAS). We quantified the type and concentration of defects in polycrystalline bulk Cr_2O_3 samples by carrying out PAS measurements,[48] which offer sensitivity for sparse small volume defects. By measuring the positron annihilation lifetime (PALS) components τ_i and their corresponding relative intensities I_i (i denotes the respective component number), we accessed the defect type, average defect dimensions, and their concentrations. The PALS measurements were performed at the Monoenergetic Positron Source (MePS) beamline at ELBE (HZDR, Germany).[49] Positrons in solids thermalize, diffuse, and then annihilate with core and valence electrons of the material, which results in the emission of at least two ∼511 keV gamma photons. Due to the momentum of the electrons, the variation from that value is a result of Doppler broadening of the annihilation line. The Doppler broadening is characterized by the so-called shape parameter S,[50,51] which is typically more sensitive to the concentration of open volume defects. The depth sensitivity is given by the variation of the positron incident energy, E_p. The setup allows for the positron energy E_p to be tuned from 0.05 to 35 keV. The energy resolution of the high purity Ge detector at 511 keV is 1.09(1) keV, resulting in a high sensitivity to changes in the material defect nanostructure from the surface to depth. To analyze the experimental data, the positron stopping profiles are approximated by a Makhovian distribution, and the mean positron penetration depth is $\langle z \rangle = A\rho^{-1}E_p^{\,n}$, where ρ is the material density and the parameters A and n are material-related constants.

Calculation of the Positron Diffusion Length L_+ Using PALSfit. The $S(E_p)$ dependence is fitted with the VEPFIT code[52] to calculate the effective diffusion lengths, L_+. This parameter is inversely proportional to the defect concentration c_V. The code allows one to fit the $S(E_p)$ curves for single and multilayered films and to acquire thicknesses, L_+, and specific S-parameters for each layer within a stack. In this work, we analyzed the data for a homogeneous material and determined that $L_+ = 99.1 \pm 0.6$ nm and $S = 0.4973(2)$. The calculated S-parameter coincides with the experimentally determined bulk value (Figure S6a), and L_+ is in the range for a defect free material. The material density $[\rho(Cr_2O_3)]$ of 5.22 g·cm^{-3} was utilized for the calculations.

Evaluation of the Defect Concentration Based on the Positron Diffusion Length. We assume a single major defect type in the sample (vacancy complex as indicated by PALS), which leads to the vacancy concentration c_V:[53] $c_V = [(L_{+,B}/L_+)^2 - 1]/(\upsilon_V \tau_B)$, where υ_V is a specific positron trapping rate (trapping coefficient) and τ_B (= 0.1517 ns) and $L_{+,B}$ (= 130 nm) are the bulk lifetime and the diffusion length in a defect free material. The typical specific positron trapping rate (υ_V) is ≈1×10^{15} s^{-1} [54] for single vacancies and N·υ_V for an N number of vacancies within a complex.[55] In our case, an N of 7 is estimated. Hence, υ_V of ≈7×10^{15} s^{-1} was taken to calculate the defect concentration of c_V (≈ 0.66 ppm).

Nitrogen Vacancy (NV) Magnetometry. NV magnetometry makes use of the electronic spin triplet ground state of the atomic NV defect in the diamond to measure stray fields on the nanoscale.[27] A small bias field (<60 Oe) is applied along the NV axis (54° from the sample normal) to split the $m_s = |\pm 1\rangle$ states of the NV. The magnetic stray field along the NV axis is then proportional to the Zeeman splitting of the $m_s = |\pm 1\rangle$ states, allowing us to achieve quantitative

https://doi.org/10.1021/acsaelm.2c00398
ACS Appl. Electron. Mater. 2022, 4, 2943−2952

nanoscale imaging. For imaging, a single NV center is located at the tip of an all-diamond scanning probe[28] to provide scanning magnetometry capabilities with ~50 nm spatial resolution. The imaging is performed using feedback to lock to one of the NV resonances,[56] thereby extracting the local stray field.

■ ASSOCIATED CONTENT

Supporting Information

The Supporting Information is available free of charge at https://pubs.acs.org/doi/10.1021/acsaelm.2c00398.

Additional information on the structural and magnetic characterization of the samples including X-ray diffraction, transmission electron microscopy, energy dispersive X-ray spectroscopy, composition analysis, positron annihilation spectroscopy data, and temperature evolution of the antiferromagnetic domain pattern taken with scanning nitrogen vacancy magnetometry (PDF)

■ AUTHOR INFORMATION

Corresponding Authors

Igor Veremchuk − *Helmholtz-Zentrum Dresden-Rossendorf e.V., Institute of Ion Beam Physics and Materials Research, Dresden 01328, Germany*; Email: i.veremchuk@hzdr.de

Denys Makarov − *Helmholtz-Zentrum Dresden-Rossendorf e.V., Institute of Ion Beam Physics and Materials Research, Dresden 01328, Germany*; orcid.org/0000-0002-7177-4308; Email: d.makarov@hzdr.de

Authors

Pavlo Makushko − *Helmholtz-Zentrum Dresden-Rossendorf e.V., Institute of Ion Beam Physics and Materials Research, Dresden 01328, Germany*

Natascha Hedrich − *Department of Physics, University of Basel, Basel 4056, Switzerland*; orcid.org/0000-0002-8742-5567

Yevhen Zabila − *Helmholtz-Zentrum Dresden-Rossendorf e.V., Institute of Ion Beam Physics and Materials Research, Dresden 01328, Germany*

Tobias Kosub − *Helmholtz-Zentrum Dresden-Rossendorf e.V., Institute of Ion Beam Physics and Materials Research, Dresden 01328, Germany*

Maciej Oskar Liedke − *Helmholtz-Zentrum Dresden-Rossendorf e.V., Institute of Radiation Physics, Dresden 01328, Germany*

Maik Butterling − *Helmholtz-Zentrum Dresden-Rossendorf e.V., Institute of Radiation Physics, Dresden 01328, Germany*

Ahmed G. Attallah − *Helmholtz-Zentrum Dresden-Rossendorf e.V., Institute of Radiation Physics, Dresden 01328, Germany*; orcid.org/0000-0002-7759-0315

Andreas Wagner − *Helmholtz-Zentrum Dresden-Rossendorf e.V., Institute of Radiation Physics, Dresden 01328, Germany*

Ulrich Burkhardt − *Max-Planck-Institut für Chemische Physik fester Stoffe, 01187 Dresden, Germany*

Oleksandr V. Pylypovskyi − *Helmholtz-Zentrum Dresden-Rossendorf e.V., Institute of Ion Beam Physics and Materials Research, Dresden 01328, Germany; Kyiv Academic University, 03142 Kyiv, Ukraine*; orcid.org/0000-0002-5947-9760

René Hübner − *Helmholtz-Zentrum Dresden-Rossendorf e.V., Institute of Ion Beam Physics and Materials Research, Dresden 01328, Germany*; orcid.org/0000-0002-5200-6928

Juergen Fassbender − *Helmholtz-Zentrum Dresden-Rossendorf e.V., Institute of Ion Beam Physics and Materials Research, Dresden 01328, Germany*

Patrick Maletinsky − *Department of Physics, University of Basel, Basel 4056, Switzerland*; orcid.org/0000-0003-1699-388X

Complete contact information is available at: https://pubs.acs.org/10.1021/acsaelm.2c00398

Author Contributions

SPS synthesis and PXRD characterization were carried out by I.V. EBSD characterization was done by U.B. The PAS and PALS studies and data analysis were performed by M.O.L., M.B., A.G.A., and A.W. with support from I.V. and P.M. The magnetotransport studies were carried out and analyzed by P.M., T.K., and I.V. with support from O.V.P. and D.M. NV magnetometry was measured and analyzed by N.H. and P.M. with support from O.V.P., P.M., and D.M. Magnetoelectric characterization was performed by I.V. and Y.Z. TEM measurements were done by R.H. SQUID-VSM data was taken by P.M. The manuscript was written by I.V. and D.M. with support from all coauthors. D.M., I.V., P.M., and J.F. conceived the project. All authors have given approval to the final version of the manuscript.

Funding

This work was partially supported by the Impulse- und Networking fund of the Helmholtz Association (FKZ VH-VI-442 Memriox) and the Helmholtz Energy Materials Characterization Platform (03ET7015). This work was financed in part via the German Research Foundation (DFG) Grants No. MA5144/22-1 and MA5144/24-1 and Helmholtz Association of German Research Centers in the frame of the Helmholtz Innovation Lab "FlexiSens". Furthermore, the funding of TEM Talos by the German Federal Ministry of Education and Research (BMBF), Grant No. 03SF0451, in the framework of HEMCP is acknowledged.

Notes

The authors declare no competing financial interest.

■ ACKNOWLEDGMENTS

We thank Annette Kunz (HZDR) for the TEM specimen preparation. Support by the Max Planck Institute for Chemical Physics and Solids and personally Prof. Yuri Grin is gratefully acknowledged. Support by the Ion Beam Center and ELBE large-scale facilities at the HZDR is gratefully acknowledged. We thank Dr. Shengqiang Zhou (HZDR) for his support with the SQUID-VSM characterization. We thank Dr. Brendan Shields and Dr. Kai Wagner (both University of Basel) for their support with NV microscopy measurements and fruitful discussions.

■ ABBREVIATIONS

SPS, spark plasma sintering; TEM, transmission electron microscopy; SEM, scanning electron microscopy; EDXS, energy dispersive X-ray spectroscopy; DFT, density functional theory; PAS, positron annihilation spectroscopy; PALS, positron annihilation lifetime spectroscopy; NV, nitrogen vacancy; SQUID-VSM, superconductive quantum interference device vibrating sample magnetometry; MERAM, magnetoelectric random access memory; PXRD, powder X-ray diffraction; HAADF-STEM, high-angle annular dark-field

scanning transition electron microscopy; EBSD, electron backscatter diffraction; FIB, focused ion beam

REFERENCES

(1) Fiebig, M. Revival of the Magnetoelectric Effect. *J. Phys. D: Appl. Phys.* **2005**, *38*, R123−R152.
(2) Astrov, D. N. Magnetoelectric Effect in Chromium Oxide. *J. Exp. Theor. Phys.* **1961**, *13*, 729−733; *Soviet Phys. JETP* **1961**, *40*, 1035−1041.
(3) He, X.; Wang, Y.; Wu, N.; Caruso, A. N.; Vescovo, E.; Belashchenko, K. D.; Dowben, P. A.; Binek, C. Robust Isothermal Electric Control of Exchange Bias at Room Temperature. *Nat. Mater.* **2010**, *9*, 579−585.
(4) Kosub, T.; Kopte, M.; Hühne, R.; Appel, P.; Shields, B.; Maletinsky, P.; Hübner, R.; Liedke, M. O.; Fassbender, J.; Schmidt, O. G.; Makarov, D. Purely Antiferromagnetic Magnetoelectric Random Access Memory. *Nature Commun.* **2017**, *8*, 13985.
(5) Hedrich, N.; Wagner, K.; Pylypovskyi, O. V.; Shields, B. J.; Kosub, T.; Sheka, D. D.; Makarov, D.; Maletinsky, P. Nanoscale Mechanics of Antiferromagnetic Domain Walls. *Nat. Phys.* **2021**, *17*, 574−577.
(6) Mahmood, A.; Echtenkamp, W.; Street, M.; Wang, J.-L.; Cao, S.; Komesu, T.; Dowben, P. A.; Buragohain, P.; Lu, H.; Gruverman, A.; Parthasarathy, A.; Rakheja, S.; Binek, C. Voltage Controlled Néel Vector Rotation in Zero Magnetic Field. *Nature Commun.* **2021**, *12*, 1674.
(7) Wadley, P.; Howells, B.; Železný, J.; Andrews, C.; Hills, V.; Campion, R. P.; Novák, V.; Olejník, K.; Maccherozzi, F.; Dhesi, S. S.; Martin, S. Y.; Wagner, T.; Wunderlich, S.; Freimuth, F.; Mokrousov, Y.; Kuneš, J.; Chauhan, J. C.; Grzybowski, M. J.; Rushforth, A. W.; Edmonds, K. W.; Gallagher, B. L.; Jungwirth, T. Electrical switching of an antiferromagnet. *Science* **2016**, *351*, 587−590.
(8) Železný, J.; Gao, H.; Výborný, K.; Zemen, J.; Mašek, J.; Manchon, A.; Wunderlich, J.; Sinova, J.; Jungwirth, T. Relativistic Néel-Order Fields Induced by Electrical Current in Antiferromagnets. *Phys. Rev. Lett.* **2014**, *113*, 157201.
(9) Moriyama, T.; Oda, K.; Ohkochi, T.; Kimata, M.; Ono, T. Spin torque control of antiferromagnetic moments in NiO. *Sci. Rep.* **2018**, *8*, 14167.
(10) Yan, H.; Feng, Z.; Qin, P.; Zhou, X.; Guo, H.; Wang, X.; Chen, H.; Zhang, X.; Wu, H.; Jiang, C.; Liu, Z. Electric-Field-Controlled Antiferromagnetic Spintronic Devices. *Adv. Mater.* **2020**, *32*, 1905603.
(11) Shtrikman, S.; Treves, D. Observation of the Magnetoelectric Effect in Cr_2O_3 Powders. *Phys. Rev.* **1963**, *130*, 986−988.
(12) Liu, Y. Y.; Xie, S. H.; Li, J. Y. The Effective Medium Approximation for Annealed Magnetoelectric Polycrystals. *J. Appl. Phys.* **2008**, *103*, 023919.
(13) Liu, Y. Y.; Xie, S. H.; Jin, G.; Li, J. Y. The Effective Magnetoelectric Coefficients of Polycrystalline Cr_2O_3 Annealed in Perpendicular Electric and Magnetic Fields. *J. Appl. Phys.* **2009**, *105*, 073917.
(14) Jungwirth, T.; Marti, X.; Wadley, P.; Wunderlich, J. Antiferromagnetic Spintronics. *Nat. Nanotechnol.* **2016**, *11*, 231−241.
(15) Baltz, V.; Manchon, A.; Tsoi, M.; Moriyama, T.; Ono, T.; Tserkovnyak, Y. Antiferromagnetic Spintronics. *Rev. Mod. Phys.* **2018**, *90*, 015005.
(16) Cura, M. E.; Singh, V. K.; Viitaharju, P.; Lehtonen, J.; Hannul, S.-P. Pulsed Electric Current Sintered Cr_2O_3-rGO Composites. *Key Engineering Materials* **2016**, *721*, 419−424.
(17) Ownby, P. D.; Jungquist, G. E. Final Sintering of Cr_2O_3. *J. Am. Ceram. Soc.* **1972**, *55*, 433−436.
(18) Munir, Z. A.; Anselmi-Tamburini, U.; Ohyanagi, M. The Effect of Electric Field and Pressure on the Synthesis and Consolidation of Materials: A Review of the Spark Plasma Sintering Method. *J. Mater. Sci.* **2006**, *41*, 763−777.
(19) Orru, R.; Richeri, R.; Locci, A. M.; Cincotti, A.; Cao, G. Consolidation/Synthesis of Materials by Electric Current Activated/Assisted Sintering. *Mater. Sci. Eng. R* **2009**, *63*, 127−287.
(20) Pravarthana, D.; Chateigner, D.; Lutterotti, L.; Lacotte, M.; Marinel, S.; Dubos, P. A.; Hervas, I.; Hug, E.; Salvador, P. A.; Prellier, W. Growth and Texture of Spark Plasma Sintered Al_2O_3 Ceramics: A Combined Analysis of X-rays and Electron Back Scatter Diffraction. *J. Appl. Phys.* **2013**, *113*, 153510.
(21) Carter, C. B.; Norton, M. G. *Ceramic Materials: Science and Engineering*; Springer Science, 2007.
(22) Pinto, H. P.; Nieminen, R. M.; Elliott, S. D. Ab Initio Study of γ−Al_2O_3 Surfaces. *Phys. Rev. B* **2004**, *70*, 125402.
(23) Marmier, A.; Lozovoi, A.; Finnis, M. W. The α-Alumina (0001) Surface: Relaxations and Dynamics from Shell Model and Density Functional Theory. *J. Eur. Ceram. Soc.* **2003**, *23*, 2729−2735.
(24) Blonski, S.; Garofalini, S. H. Molecular Dynamics Simulations of α-Alumina and γ-Alumina Surfaces. *Surf. Sci.* **1993**, *295*, 263−274.
(25) Guilmeau, E.; Henrist, C.; Suzuki, T. S.; Sakka, Y.; Chateigner, D.; Grossin, D.; Ouladdiaf, B. Texture of Alumina by Neutron Diffraction and SEM-EBSD. *Mater. Sci. Forum* **2005**, *495*−*497*, 1395−1400.
(26) McGuire, T. R.; Scott, E. J.; Grannis, F. H. Antiferromagnetism in a Cr_2O_3 Crystal. *Phys. Rev.* **1956**, *102*, 1000−1003.
(27) Rondin, L.; Tetienne, J.-P.; Hingant, T.; Roch, J.-F.; Maletinsky, P.; Jacques, V. Magnetometry with Nitrogen-Vacancy Defects in Diamond. *Rep. Prog. Phys.* **2014**, *77*, 056503.
(28) Hedrich, N.; Rohner, D.; Batzer, M.; Maletinsky, P.; Shields, B. J. Parabolic Diamond Scanning Probes for Single-Spin Magnetic Field Imaging. *Phys. Rev. Appl.* **2020**, *14*, 064007.
(29) Wörnle, M. S.; Welter, P.; Giraldo, M.; Lottermoser, T.; Fiebig, M.; Gambardella, P.; Degen, C. L. Coexistence of Bloch and Néel Walls in a Collinear Antiferromagnet. *Phys. Rev. B* **2021**, *103*, 094426.
(30) Appel, P.; Shields, B. J.; Kosub, T.; Hedrich, N.; Hübner, R.; Faßbender, J.; Makarov, D.; Maletinsky, P. Nanomagnetism of Magnetoelectric Granular Thin-Film Antiferromagnets. *Nano Lett.* **2019**, *19*, 1682−1687.
(31) Hoser, A.; Köbler, U. *Renormalization Group Theory*; Springer: Berlin, Heidelberg, 2012.
(32) Kosub, T.; Kopte, M.; Radu, F.; Schmidt, O. G.; Makarov, D. All-Electric Access to the Magnetic-Field-Invariant Magnetization of Antiferromagnets. *Phys. Rev. Lett.* **2015**, *115*, 097201.
(33) Iino, T.; Moriyama, T.; Iwaki, H.; Aono, H.; Shiratsuchi, Y.; Ono, T. Resistive Detection of the Néel Temperature of Cr_2O_3 Thin Films. *Appl. Phys. Lett.* **2019**, *114*, 022402.
(34) Miura, K.; Fujiwara, K.; Shiogai, J.; Nojima, T.; Tsukazaki, A. Electrical Detection of the Antiferromagnetic Transition in $MnTiO_3$ Ultrathin Films by Spin Hall Magnetoresistance. *J. Appl. Phys.* **2020**, *127*, 103903.
(35) Oda, K.; Moriyama, T.; Kimata, M.; Kasukawa, S.; Ono, T. Temperature Dependence of Spin Hall Magnetoresistance across the Néel Temperature of CoO. *Jpn. J. Appl. Phys.* **2020**, *59*, 010908.
(36) Schlitz, R.; Kosub, T.; Thomas, A.; Fabretti, S.; Nielsch, K.; Makarov, D.; Goennenwein, S. T. B. Evolution of the Spin Hall Magnetoresistance in Cr_2O_3/Pt Bilayers Close to the Néel Temperature. *Appl. Phys. Lett.* **2018**, *112*, 132401.
(37) Wang, J.-L.; Echtenkamp, W.; Mahmood, A.; Binek, C. Voltage Controlled Magnetism in Cr_2O_3 Based All-Thin-Film Systems. *J. Magn. Magn. Mater.* **2019**, *486*, 165262.
(38) Moriyama, T.; Shiratsuchi, Y.; Lino, T.; Aono, H.; Suzuki, M.; Nakamura, T.; Kotani, Y.; Nakatani, R.; Nakamura, K.; Ono, T. Giant Anomalous Hall Conductivity at the Pt/Cr_2O_3 Interface. *Phys. Rev. Appl.* **2020**, *13*, 034052.
(39) Veremchuk, I.; Liedke, M. O.; Makushko, P.; Kosub, T.; Hedrich, N.; Pylypovskyi, O. V.; Ganss, F.; Butterling, M.; Hübner, R.; Hirschmann, E.; Attallah, A. G.; Wagner, A.; Wagner, K.; Shields, B.; Maletinsky, P.; Fassbender, J.; Makarov, D. Defect Nanostructure and its Impact on Magnetism of α-Cr_2O_3 Thin Films. *Small* **2022**, *18*, 2201228.
(40) Dzyaloshinskii, I. E. On the Magneto-Electrical Effect in Antiferromagnets. *J. Exp. Theor. Phys.* **1959**, *37*, 881−882; *Soviet Phys. JETP* **1960**, *10*, 628−629.

https://doi.org/10.1021/acsaelm.2c00398
ACS Appl. Electron. Mater. 2022, 4, 2943−2952

(41) Ashida, T.; Oida, M.; Shimomura, N.; Nozaki, T.; Shibata, T.; Sahashi, M. Observation of Magnetoelectric Effect in Cr_2O_3/Pt/Co Thin Film System. *Appl. Phys. Lett.* **2014**, *104*, 152409.
(42) Punugupati, S.; Narayan, J.; Hunte, F. Room Temperature Ferromagnetism in Epitaxial Cr_2O_3 Thin Films Grown on r-Sapphire. *J. Appl. Phys.* **2015**, *117*, 193907.
(43) Punugupati, S.; Narayan, J.; Hunte, F. Strain Induced Ferromagnetism in Epitaxial Cr_2O_3 Thin Films Integrated on Si(001). *Appl. Phys. Lett.* **2014**, *105*, 132401.
(44) Ye, S.; Shiokawa, Y.; Pati, S. P.; Sahashi, M. Parasitic Magnetism in Magnetoelectric Antiferromagnet. *ACS Appl. Mater. Interfaces* **2020**, *12*, 29971−29978.
(45) Ye, S.; Shiokawa, Y.; Pati, S. P.; Sahashi, M. Spin Reversal Mechanism of a Perpendicular Exchange Bias System with an Antiferromagnet Incorporating a Parasitic Ferromagnetism. *Physica Status Solidi (RRL) − Rapid Research Letters* **2019**, *13*, 1900135.
(46) He, X.; Echtenkamp, W.; Binek, C. Scaling of the magnetoelectric effect in chromia thin films. *Ferroelectrics* **2012**, *426*, 81−89.
(47) Akselrud, L.; Grin, Yu. WinCSD: Software Package for Crystallographic Calculations (Version 4). *J. Appl. Crystallogr.* **2014**, *47*, 803−805.
(48) Tuomisto, F.; Makkonen, I. Defect Identification in Semiconductors with Positron Annihilation: Experiment and Theory. *Rev. Mod. Phys.* **2013**, *85*, 1583−1631.
(49) Wagner, A.; Butterling, M.; Liedke, M. O.; Potzger, K.; Krause-Rehberg, R. Positron Annihilation Lifetime and Doppler Broadening Spectroscopy at the ELBE Facility. *AIP Conf. Proc.* **2017**, *1970*, 040003.
(50) Liedke, M. O.; Anwand, W.; Bali, R.; Cornelius, S.; Butterling, M.; Trinh, T. T.; Wagner, A.; Salamon, S.; Walecki, D.; Smekhova, A.; Wende, H.; Potzger, K. Open Volume Defects and Magnetic Phase Transition in $Fe_{60}Al_{40}$ Transition Metal Aluminide. *J. Appl. Phys.* **2015**, *117*, 163908.
(51) Krause-Rehberg, R.; Leipner, H. S. *Positron Annihilation in Semiconductors: Defect Studies*; Springer: Berlin Heidelberg, 1999.
(52) van Veen, A.; Schut, H.; Clement, M.; de Nijs, J. M. M.; Kruseman, A.; IJpma, M. R. VEPFIT Applied to Depth Profiling Problems. *Appl. Surf. Sci.* **1995**, *85*, 216.
(53) Čížek, J.; Lukáč, F.; Procházka, I.; Kužel, R.; Jirásková, Y.; Janičkovič, D.; Anwand, W.; Brauer, G. Characterization of Quenched-in Vacancies in Fe−Al Alloys. *Phys. B: Condens. Matter.* **2012**, *407*, 2659−2664.
(54) Saarinen, K.; Hautojärvi, P.; Corbel, C. Chapter 5: Positron Annihilation Spectroscopy of Defects in Semiconductors. In *Semicond. Semimetals*; Elsevier, 1998; pp 209−285.
(55) Nieminen, R. M.; Laakkonen, J. Positron Trapping Rate into Vacancy Clusters. *Appl. Phys.* **1979**, *20*, 181−184.
(56) Schoenfeld, R.; Harneit, W. Real Time Magnetic Field Sensing and Imaging using a Single Spin in Diamond. *Phys. Rev. Lett.* **2011**, *106*, 030802.

https://doi.org/10.1021/acsaelm.2c00398
ACS Appl. Electron. Mater. 2022, 4, 2943−2952